



Electronic properties of a graphyne- N monolayer and its multilayer: Even-odd effect and topological nodal line semimetallic phases

Takuto Kawakami ^{*}, Takafumi Nomura, and Mikito Koshino 
Department of Physics, Osaka University, Toyonaka, Osaka 560-0043, Japan



(Received 26 August 2020; accepted 30 August 2020; published 18 September 2020)

We study the electronic structure and topological properties of monolayer and the ABC-stacked multilayer of graphyne- N , which are a family of planar carbon sheets consisting of sp and sp_2 -bonding. By using the density-functional theory and the effective continuum model, we find a striking even-odd effect in the dependence of the band structure on N (the number of carbon-carbon triple bonds between neighboring benzene rings). Specifically, the even- N graphyne monolayer has doubly degenerate conduction and valence bands near the Fermi energy, and in its ABC multilayer, the band inversion of the doubly degenerate bands leads to a nodal-line semimetal phase with nontrivial \mathbb{Z}_2 monopole charge. In contrast, the odd- N monolayer has singly degenerate bands in separate valleys, and its ABC multilayer can have only \mathbb{Z}_2 -trivial nodal lines. ABC graphynes with larger N tend to be trivial insulators because of smaller interlayer coupling, while the external pressure induces a topological phase transition from the trivial phase to the nodal line semimetal phase.

DOI: [10.1103/PhysRevB.102.115421](https://doi.org/10.1103/PhysRevB.102.115421)

I. INTRODUCTION

Carbon allotropes have attracted much attention because of their variety of topological properties depending on the atomic configurations. The best-known example is graphene, where a honeycomb lattice of carbon atoms constructed by sp_2 covalent bonds [1] gives rise to a symmetry-protected band touching with a linear dispersion [2,3]. The sp -based one-dimensional (1D) carbon chain, carbyne [4], is known to be a 1D topological insulator described by the Su-Schrieffer-Heeger model [5,6]. Other types of pure carbon materials have also been studied from a viewpoint of topological phenomena [7–24].

Furthermore, there is another class of carbon allotropes called graphyne, which can be regarded as a hybrid of graphene and carbyne. A graphyne generally takes a two-dimensional planar structure purely composed of carbon atoms with a mixture of sp_2 and sp bonds [25–31]. Figure 1 shows representative structures called the graphyne- N family, which is defined as a triangle lattice of benzene rings connected by polyyne chains with N triple bonds ($C\equiv C$). The band calculation shows that monolayer graphyne- N 's are semiconductors with band gaps about a few hundred meV [26,27].

Recently, significant progress was made on the experimental studies on graphyne-2 (or called graphdiyne) [32,33]. Particularly, a high-quality three-dimensional stack of graphyne-2 was successfully synthesized, and it was identified as ABC rhombohedral structure by x-ray diffraction measurement [33]. Theoretically, two of the present authors found that ABC-stacked graphyne-2 is a topological nodal line semimetal with band-touching nodal loops, and derived an

effective continuum model for its low-energy band structure [34]. Then it was pointed out that the nodal line of ABC-graphyne-2 was characterized by a nontrivial \mathbb{Z}_2 monopole charge [35]. A \mathbb{Z}_2 -nontrivial nodal loop cannot disappear in its own, but it can only pair-annihilate with the other loop [36,37]. In recent years, various materials with nodal lines were theoretically proposed and some of them were experimentally probed [15,37–88]. Nevertheless, to the best of our knowledge, the nontrivial \mathbb{Z}_2 monopole charge [36] is still elusive in nature. So far it is known only in ABC-stacked graphyne-2 [35] and transition metal dichalcogenide [85,86].

These nontrivial properties of graphyne-2 motivates us to generalize the theoretical analysis to other types of graphyne- N . In this paper, we study the electronic structure and the topological property of the general graphyne- N monolayer and its three-dimensional ABC stack, by using the density functional theory (DFT) and the effective continuum model. We demonstrate that the band structure is significantly different between even N 's and odd N 's. First, we show that even- N graphyne monolayer has doubly degenerate conduction and valence bands near the Fermi energy, while odd- N graphyne monolayer only has singly degenerate bands in separate valleys. Such the even-odd effect is crucial in the topological nature in ABC-stacked multilayers. In ABC even- N graphynes, the band inversion of doubly degenerate bands in monolayer leads to a \mathbb{Z}_2 -nontrivial nodal-line semimetal phase. In contrast, the ABC odd- N graphynes can only have \mathbb{Z}_2 -trivial nodal lines. The ABC graphynes with $N \geq 3$ become trivial insulators because of smaller interlayer coupling, while we demonstrate that the external pressure induces band inversion and topological phase transition to the nodal line semimetal phase.

This paper is organized as follows. In Sec. II, we study the band structure of monolayer graphyne- N systematically in terms of DFT calculations and tight-binding model, and

^{*}t.kawakami@qp.phys.sci.osaka-u.ac.jp

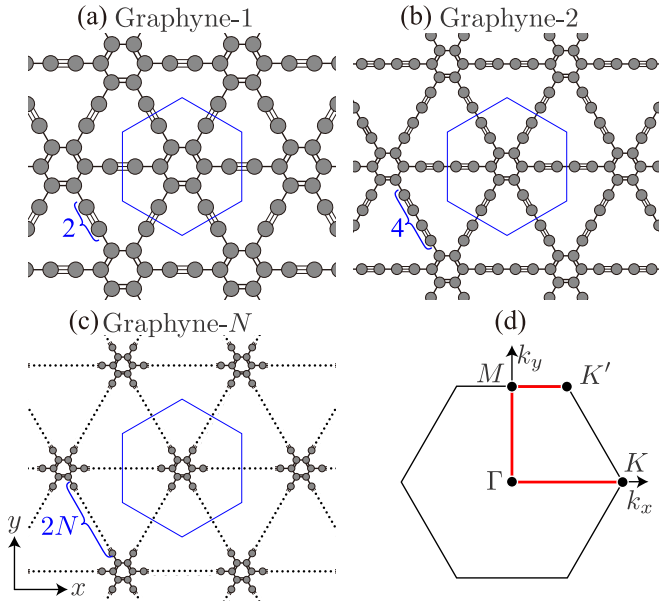


FIG. 1. (a) Lattice structures of monolayer graphyne-1, (b) -2, and (c) - N , with a unit cell indicated by a blue hexagon. (d) Brillouin zone and the high-symmetry line along which the band calculation is performed.

describe the even-odd effect of the band structure from the symmetry consideration. We investigate the band structures of ABC-stacked graphynes for even and odd N in Secs. III and IV, respectively, where the emergence of the nodal-line semimetal phase is argued from the symmetrical point of view. Finally, a brief summary is presented in Sec. V.

II. MONOLAYER GRAPHYNES

A. Band structure

We first examine the band structures and the symmetrical properties of monolayer graphyne- N . The lattice structures of monolayer graphyne-1, 2, \dots , N are displayed in Fig. 1. In graphyne- N , benzene rings are connected by 1D polyyne chains ($-\text{C}\equiv\text{C}-$) $_N$ to form a triangular lattice. The system has the point-group symmetry D_{6h} , which is generated by inversion I , sixfold rotation C_{6z} around the z axis, and twofold rotation C_{2x} around x . Hereafter C_{nq} denotes an n -fold rotation around the q axis.

We calculate the atomic and electronic structures of graphyne- $N = 1, 2, 3$, and 4 using the first-principles calculation package QUANTUM ESPRESSO [89] (see Appendix A for the details of the calculation). Figure 2 plots the electronic bands in the optimized atomic structure along the high symmetry lines in the Brillouin zone illustrated in Fig. 1(d). We see that the graphynes from $N = 1$ to 4 are all semiconductors with band gaps of a few 100 meV [27], while we observe a characteristic even-odd effect in the low-energy band structure. For even N [Figs. 2(b) and 2(d)], a gap minimum occurs at the Γ point. The band edge states are characterized as the E_{2u} and E_{1g} representation of point group D_{6h} , which have double degeneracy with odd and even parities, respectively, for inversion I . For odd N , on the other hand, the gap minimum is located at the M point, where the symmetry is D_{2h}

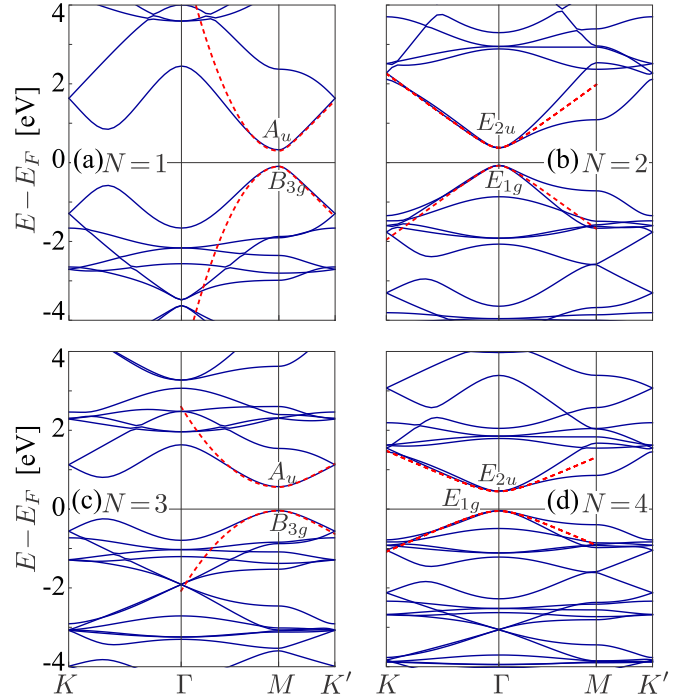


FIG. 2. Band structures of monolayer graphyne of $N = 1, 2, 3$, and 4 obtained from the DFT calculation. The dashed curve is the dispersion relation calculated by the effective continuum model (see the text).

[Figs. 2(a) and 2(c)]. The band edge states are the A_u and B_{3g} representation, and they have the same parity under rotation C_{2x} while opposite parities under inversion I and C_{2z} .

These band structures are well reproduced by single-orbital tight-binding models as shown below. As graphyne- N is a planar sheet, we have the mirror reflection symmetry M_z with respect to the xy -plane, and hence p_z atomic orbitals with odd mirror parity are decoupled from s , p_x , and p_y orbitals with even mirror parity. The latter three orbitals form the sp^2 and sp covalent bonds in the benzene rings and the 1D chain, respectively, resulting in a large band gap at the Fermi energy. Therefore, the band structure around the Fermi energy originates from p_z atomic orbitals.

Based on this argument, we construct a tight-binding model for the p_z atomic orbital on the carbon sites in Fig. 1. We take into account only the nearest-neighbor hoppings t_0, t_1, t_2, \dots , in Fig. 1, and define them by

$$t_i = t_\pi \exp(-a_i/\lambda), \quad (1)$$

where a_i is the corresponding carbon-carbon distance obtained from the optimized atomic-structure in the first-principles calculation, $\lambda = 0.9 \text{ \AA}$ is the decay length of the hopping integral, and $t_\pi = 13.1 \text{ eV}$. The parameters t_π and λ are determined to reproduce the graphene's energy band [20,90–92]. In Table I, we provide the list of the bond distance a_i for graphyne- N with $N = 1, 2, 3, 4$. The a_i varies from 1.22 to 1.42 \AA depending on the position. Accordingly, the corresponding hopping integral t_i varies from 2.7 to 3.4 eV.

In Fig. 3, we present the band structures obtained from the nearest-neighbor tight-binding model with Eq. (1). We see

TABLE I. Numerically obtained atomic distance in the monolayer graphyne- N . $a_0 = x_1 - L/2$ and $a_i = x_{i+1} - x_i$ ($i > 1$) are the distances of carbons in benzene rings and in polyne chain [see also Fig. 4(a) for the definition].

N	Atomic distance [\AA]					
	a_0	a_1	a_2	a_3	a_4	a_5
1	1.41	1.39	1.22			
2	1.42	1.38	1.23	1.33		
3	1.41	1.39	1.22	1.33	1.23	
4	1.41	1.38	1.23	1.32	1.24	1.31

that the tight-binding model captures the main features of DFT band calculations in Fig. 2 around the Fermi energy.

B. Origin of even-odd effect

The even-odd effect in the band structure of graphyne- N can be understood using the tight-binding model introduced above. As depicted in Fig. 4(a), graphyne- N can be divided into isolated 1D chains consisting of $2N + 2$ carbon atoms, by turning off the hopping t_0 in the benzene ring. The whole system can be viewed as an effective tight-binding model, with each 1D chain as an effective site, and t_0 as hopping between neighboring effective sites. For simplicity, we assume that the all the distances between neighboring atoms a_0, a_1, a_2, \dots , are equal (denoted by a), and hence all the hopping parameters t_0, t_1, t_2, \dots , are all equal (denoted by t). Here we take the origin at the center of the chain, and define the position of j th atom as $x_j = [j - (2N + 3)/2]a$ for $j = 1, 2, \dots, 2N + 2$.

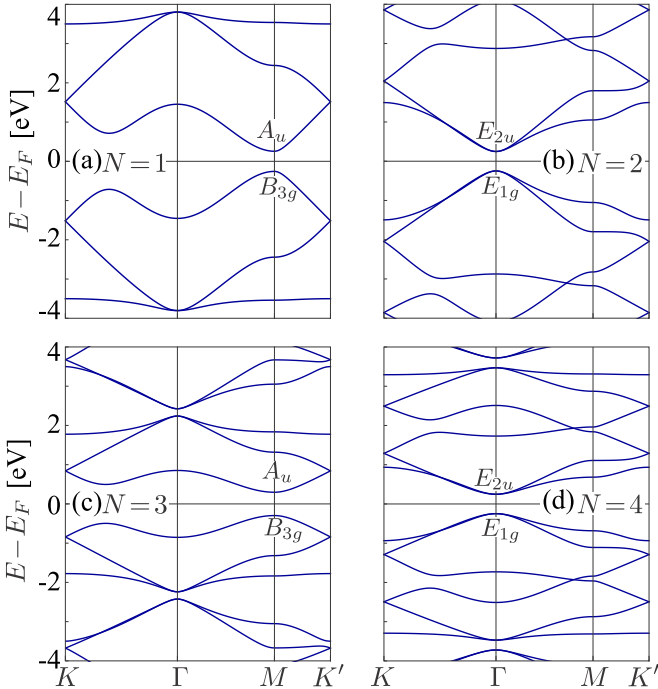


FIG. 3. Band structures of monolayer graphyne $N = 1, 2, 3$, and 4 obtained from the nearest-neighbor tight-binding model. Hopping parameters are determined by Eq. (1) with atomic distances obtained by first-principles calculation.

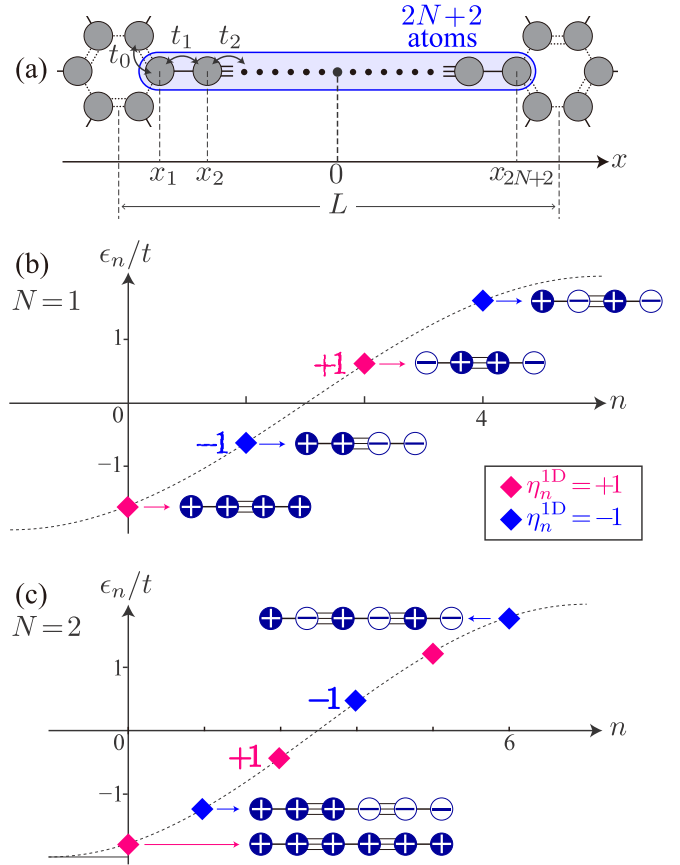


FIG. 4. (a) 1D atomic chain as a component of graphyne- N . (b) The energy levels and the schematic plot of the eigenstates (sign of the wave function on the atomic sites) for chain of $N = 1$ and (c) $N = 2$. Color of each energy level indicates the parity η_n^{1D} .

The Schrödinger equation for the isolated chain is given by $\epsilon_n \psi_n(x_j) = -t[\psi_n(x_{j+1}) + \psi_n(x_{j-1})]$. The eigenenergy of the chain is

$$\epsilon_n = -2t \cos(k_n a), \quad (2)$$

with the quantized Bloch wave number

$$k_n = \frac{n+1}{L} \pi, \quad (3)$$

where $n = 0, 1, \dots, 2N + 1$ and $L = (2N + 3)a$, and a is the lattice spacing in the chain. The level structures for $N = 1$ and 2 are shown in Figs. 4(b) and 4(c), respectively. The wave function of the n th eigenstate is

$$\psi_n(x_j) = \sqrt{\frac{2}{2N+3}} \cos\left(k_n x_j + \frac{n\pi}{2}\right). \quad (4)$$

The parity of the 1D wave function, defined by $\psi_n(x_i) = \eta_n^{\text{1D}} \psi_n(-x_i)$, is crucial to consider the band structure of the graphyne- N . From Eq. (4), the parity of the n th eigenstates is given by

$$\eta_n^{\text{1D}} = \begin{cases} -1 & \text{for odd } n, \\ +1 & \text{for even } n. \end{cases} \quad (5)$$

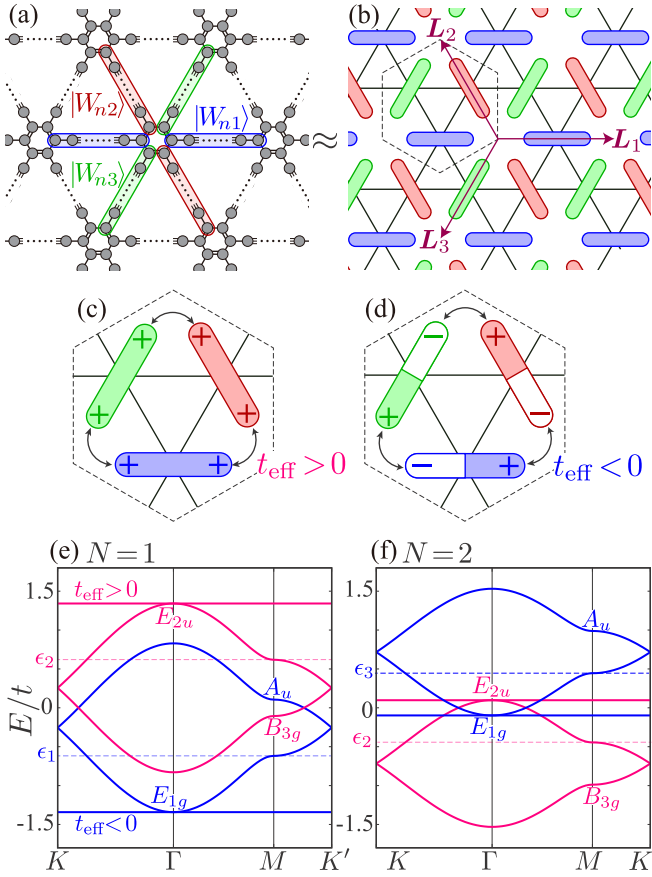


FIG. 5. (a) Decomposition of graphyne- N into 1D-chain effective sites and (b) the corresponding kagome lattice. (c) Schematics of the hopping between neighboring effective orbitals with even parity and (d) odd parity. (e) Configuration of the effective kagome bands of $n = N$ and $n = N + 1$ for graphyne $N = 1$ and (f) $N = 2$, where the mixing between different n 's is neglected.

For odd N , the states just above and below $\epsilon = 0$ has parity $\eta_n^{\text{1D}} = +1$ and -1 , respectively [Fig. 4(b)], while those for even N become $\eta_n^{\text{1D}} = -1$ and $+1$, respectively [Fig. 4(c)].

We regard these 1D chains as effective sites. They form a kagome lattice in graphyne- N as shown in Figs. 5(a) and 5(b). We define the primitive lattice vectors L_1 , L_2 , L_3 as in Fig. 5(b), where $L_3 = -L_1 - L_2$. The unit cell of the kagome lattice includes the three chains along different directions. These orbitals are expressed as $|W_{n,\alpha}(\mathbf{R}_\alpha)\rangle$ [Fig. 5(a)], where n corresponds to the n th eigenstate the 1D chain, $\alpha = 1, 2, 3$ is the index for the direction of the chain, and $\mathbf{R}_\alpha = m_1 L_1 + m_2 L_2 + L_\alpha/2$ (m_1, m_2 : integers) is the central position of the orbital α . Specifically, $|W_{n,\alpha}(\mathbf{R}_\alpha)\rangle$ is given by arranging the wave amplitudes of $\psi_n(x_1)$, $\psi_n(x_2)$, $\psi_n(x_3)$, \dots , on the atomic sites from one end to the other in the direction of L_α .

The even-odd feature of the band structure can be captured by an approximate model which takes only the matrix elements between the same n , while neglecting those between different n 's. In this approximation, the Bloch Hamiltonian of the sector n is given by $H_{n,\alpha,\beta}(\mathbf{k}) = \langle w_{n,\alpha}(\mathbf{k}) | H | w_{n,\beta}(\mathbf{k}) \rangle$,

where the Bloch state of n th orbital is defined as

$$|w_{n,\alpha}(\mathbf{k})\rangle = \sum_{\mathbf{R} \in \mathbf{R}_\alpha} \exp(i\mathbf{k} \cdot \mathbf{R}) |W_{n,\alpha}(\mathbf{R})\rangle. \quad (6)$$

When turning on the hopping in the benzene ring, the ends of the neighboring chains are coupled with each other. It gives the nearest-neighbor hopping in the effective kagome lattice. The Bloch Hamiltonian is expressed in a matrix form with the indexes α, β as

$$H_n(\mathbf{k}) = \epsilon_n \hat{1} - t_{\text{eff}} \begin{pmatrix} 0 & \cos \theta_3(\mathbf{k}) & \cos \theta_2(\mathbf{k}) \\ \cos \theta_3(\mathbf{k}) & 0 & \cos \theta_1(\mathbf{k}) \\ \cos \theta_2(\mathbf{k}) & \cos \theta_1(\mathbf{k}) & 0 \end{pmatrix}, \quad (7)$$

where $\theta_\alpha(\mathbf{k}) = \mathbf{k} \cdot \mathbf{L}_\alpha/2$ and $\hat{1}$ is a 3×3 unit matrix, and t_{eff} is the nearest-neighbor hopping in the kagome lattice, which is given by

$$\begin{aligned} t_{\text{eff}}(n) &= t \psi_n(-x_1) \psi_n(x_1) \\ &= \eta_n^{\text{1D}} \frac{2t}{2N+3} \cos^2 \frac{(2N-2n+1)\pi}{2(2N+3)}. \end{aligned} \quad (8)$$

An important point here is that the parity of the 1D-chain wave function determines the sign of $t_{\text{eff}}(n)$. As can be seen in Fig. 5(c), when the orbital has even parity $\eta_n^{\text{1D}} = +1$, the effective orbitals of the two neighboring chains have the same sign at the contact point. Therefore, the effective hopping between orbitals is $t_{\text{eff}}(n) > 0$ (noting that $t > 0$). In the same manner, we obtain $t_{\text{eff}}(n) < 0$ for the orbital with odd parity $\eta_n^{\text{1D}} = -1$ [Fig. 5(d)]. Note that the 1D modes and the associated kagome lattice were also proposed in polymerized triptycene [93].

The eigenvalues of Eq. (7) is

$$\begin{aligned} E_{nk} &= \epsilon_n + 2t_{\text{eff}}, \\ \epsilon_n - t_{\text{eff}} &\left\{ 1 \pm \left[\sum_{\alpha} [1 + 2 \cos 2\theta_\alpha(\mathbf{k})] \right]^{\frac{1}{2}} \right\}, \end{aligned} \quad (9)$$

where the first represents a flat band, and the second represents a pair of dispersive bands analog to graphene.

The effective kagome lattice clearly explains the even-odd effect of graphyne- N . For odd N , the 1D-chain eigenstates of just above and below the zero energy have even and odd parity, respectively, as shown in Fig. 4(b). These two orbitals give rise to a pair of kagome bands near the Fermi energy as depicted in Fig. 5(e). There the blue curve originates from $n = N$ state with the odd parity, and hence it has a flat band in the lower-energy side, while the magenta curve is from $n = N + 1$ state with the even parity and hence the flat band appears in the higher-energy side. In this system, the energy difference between 1D-chain orbitals, $\epsilon_{N+1} - \epsilon_N = 2|\epsilon_N|$, is smaller than the kagome band width $8|t_{\text{eff}}(N)|$ for any $N \geq 1$, so that the two kagome clusters overlap with each other, giving band crossings between K and Γ , and also between M and K' .

In the real band structure, a finite mixing between different n 's neglected in Eq. (7) induces a mini gap at these crossing points, resulting in semiconducting band structures as shown in Figs. 2(a) and 2(c). The symmetry character at the high symmetric points also depends on the parity of orbitals. For the even (odd) parity band in Fig. 5(e), the twofold-degenerate states at Γ point belong to E_{2u} (E_{1g}) representations and the

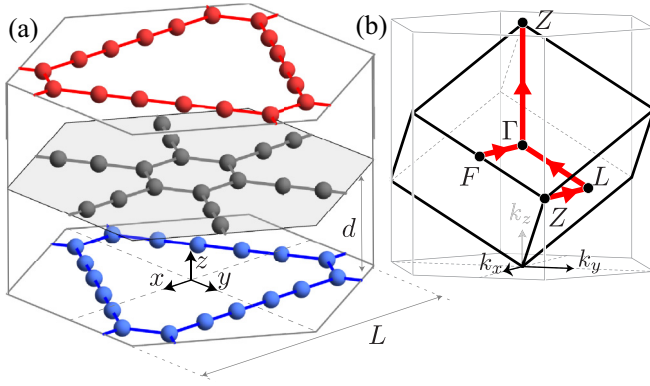


FIG. 6. (a) Lattice structure of ABC-stacked graphyne-2 and (b) the corresponding Brillouin zone.

saddle point state at M with $E_n(M) = \epsilon_n - 2t_{\text{eff}}$ to B_{3g} and (A_u) [see Appendix B for details].

In even- N , in contrast, the sign of t_{eff} becomes opposite, and therefore the low-energy kagome bands are arranged such that flat-band sides are faced to each other as in Fig. 5(f). The two sets of bands overlap in such a way that the E_{2u} states from the lower band cluster (magenta bands) has higher energy than E_{2g} from the upper band cluster (blue). The mixing between different n 's opens a band gap at the crossing points as in Figs. 2(b) and 2(d). As a result, there is a double band inversion of twofold degenerate state E_{1g} and E_{2u} , and hence the system is in a topological insulating phase. In fact, it has been pointed out that the monolayer graphyne-2 is the second-order topological insulator associated with this double band inversion [94]. Note that the similar topological phase also appears Kekulé distorted honeycomb lattice [95,96] and its counterpart in the photonic crystals [97].

III. ABC-STACKED GRAPHYNES (EVEN N)

The observation of the even-odd effects in monolayer graphyne- N motivates us to systematically study the electronic structures of three-dimensional graphyne- N . As in graphene, there are various types of stacking configurations in graphyne multilayers. Recently, x-ray diffraction experiments reported that the graphyne of $N = 2$ obtained by alkyne-alkyne homocoupling reaction takes an ABC (rhombohedral) stacking structure [33]. We investigate the electronic and topological properties of ABC-stacked graphyne of $N = 2, 4$ in this section, and that of $N = 1, 3$ in the next section.

A. ABC stacked graphyne-2

We consider the band structure and the topological property of ABC-stacked graphyne-2. In the previous works, it was found that the system has a nodal line near the Fermi energy [34], and it is characterized by a nontrivial \mathbb{Z}_2 monopole charge associated with the double band inversion [35]. In the following, we argue the origin of the double band inversion and the emergent nodal line from the viewpoint of the full crystalline symmetry.

The lattice structure of ABC-graphyne-2 is shown in Fig. 6(a). The primitive lattice vectors are given by $L_1 =$

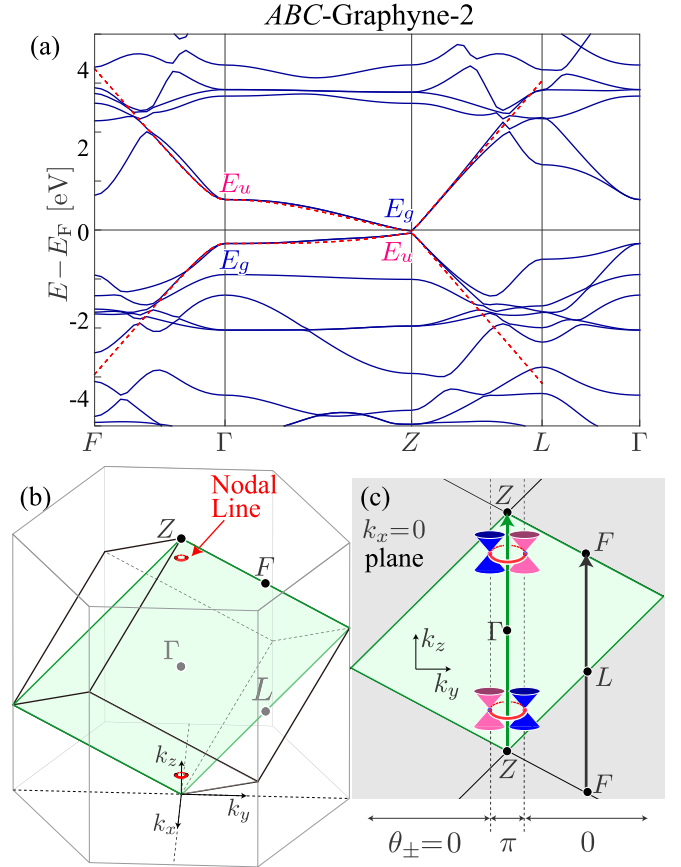


FIG. 7. (a) Band structure of ABC stacked graphyne-2 obtained from the DFT calculation. The dashed line is the dispersion relation calculated by the effective model Eq. (12). (b) The nodal line structure in the three-dimensional momentum space and (c) on $k_x = 0$ plane. In (c), the blue and magenta Dirac cones correspond to the mirror eigenvalues $\eta(M_x) = \pm 1$, respectively.

$\frac{L}{2\sqrt{3}}\hat{y} + d\hat{z}$, $L_2 = -\frac{L}{2}\hat{x} - \frac{L}{2\sqrt{3}}\hat{y} + d\hat{z}$, and $L_3 = \frac{L}{2}\hat{x} - \frac{L}{2\sqrt{3}}\hat{y} + d\hat{z}$. The first Brillouin zone is given by a rhombohedron [Fig. 11(b)]. The point-group symmetry is D_{3d} . Compared to the monolayer counterpart, the sixfold rotational symmetry C_{6z} is reduced to threefold symmetry C_{3z} , and also C_{2y} is broken.

Figure 7(a) displays the band structure of ABC graphyne-2, which is obtained from the DFT calculation with the optimized lattice structure in Fig. 6(a). The nodal lines are not located on the high-symmetry path in Fig. 7(a), but they are at off-center momenta surrounding the k_z -axis, as depicted in Fig. 7(b) [34,35]. The key factors for the emergence of the nodal lines are the band degeneracy and the double band inversion between the Γ and Z points. These two points have the D_{3d} group symmetry, and the twofold degenerate states near the Fermi energy are characterized by E_g and E_u representations, which originate from E_{1g} and E_{2u} states in the monolayer system. At the Γ point, E_u is higher than E_g in energy, while at the Z point, E_g is higher than E_u . Since E_g and E_u are even and odd under the space inversion I , respectively, we have a double band inversion between the Γ and Z points.

The $k_x = 0$ plane including the Γ and Z points is invariant under mirror reflection M_x , where the bands are labeled by

the mirror eigenvalue $\eta(M_x) = \pm 1$. At Γ and Z , each of the doublet states E_u and E_g is composed of opposite mirror eigenvalues $\eta(M_x) = +1$ and -1 . Therefore, the two sectors of $\eta(M_x) = +1$ and -1 simultaneously have a band inversion in the eigenvalue of inversion I between Γ and Z point.

On the $k_x = 0$ plane, we can define the Berry phase (Zak phase) $\theta_{\pm}(k_y)$ for each sector of $\eta(M_x) = \pm 1$, by integrating the Berry connection along the k_z axis for a span of the Brillouin zone with k_y fixed [see Fig. 7(c)]. The $\theta_{\pm}(k_y)$ is quantized to 0 or π because of the inversion and time-reversal symmetry of the present system. On the $Z\Gamma Z$ line ($k_y = 0$), the band inversion in each mirror sector ensures $\theta_{\pm}(0) = \pi$ [98]. On the line FLF ($k_y = \pi/L$), in contrast, there are no band inversions because of the large band gap, and thus $\theta_{\pm}(\pi/L) = 0$. Between the two lines $Z\Gamma Z$ and FLF , therefore, there must be a jump of the Berry phase from $\theta_{\pm}(k_y) = \pi$ to 0, at which the energy gap closes in the corresponding sector of $\eta(M_x) = \pm$. This is the cross section of the nodal line and the $k_x = 0$ plane. The $\eta(M_x) = \pm$ sectors have gap closing generally at different positions in the momentum space, as illustrated by the magenta and blue Dirac cones, respectively, in Fig. 7(c). The position of the gap closing point will be argued later in more detail. The Berry phase on an infinitesimal closed path encircling a single gap closing point is π . As the Berry phase on a closed path is always quantized to 0 or π due to the inversion and time-reversal symmetry, the gap-closing point persists even away from the $k_x = 0$ plane. This explains the nodal lines in the three-dimensional momentum space.

In the following, we derive an effective 4×4 low-energy Hamiltonian from a symmetry-based consideration for the states E_g and E_u at the Γ points. We define the four-dimensional basis as $|\alpha, \beta\rangle$ where $\alpha = \pm$ represents E_g and E_u , respectively and $\beta = \pm$ is the degree of freedom in the twofold degeneracy, corresponding to the sign of the angular momentum [see Appendix C]. In this basis, a reducible 4×4 representation of the twofold rotation and improper sixfold rotation generating of D_{3d} are

$$C_{2x} = \sigma_x \tau_0, \quad \text{and} \quad S_6 = e^{2\pi i/3\sigma_z} \tau_z. \quad (10)$$

Here, τ_i with $i = 0, x, y, z$ are the unit matrix and the Pauli matrices acting on α , while σ_i is on β . The time-reversal operator is expressed as

$$\mathcal{T} = \sigma_x \tau_z \mathcal{K}, \quad (11)$$

where \mathcal{K} is the complex conjugate operator.

The symmetry requirements for the effective Hamiltonian $H(\mathbf{k})$ are then written as $S_6 H(\mathbf{k}) S_6^{-1} = H(D_{S_6}[\mathbf{k}])$, $C_{2x} H(\mathbf{k}) C_{2x}^{-1} = H(D_{C_{2x}}[\mathbf{k}])$, and $\mathcal{T} H(\mathbf{k}) \mathcal{T}^{-1} = H(-\mathbf{k})$. Up to the first order of k_x and k_y , $H(\mathbf{k})$ is uniquely determined as

$$H(\mathbf{k}) = m_0 + m_1 \tau_z + v \tau_x (\sigma_x k_x + \sigma_y k_y) + m' \tau_y \sigma_z + (v'_1 + v'_2 \tau_z) (\sigma_y k_x - \sigma_x k_y), \quad (12)$$

where $m_0(k_z)$, $m_1(k_z)$, and $v(k_z)$ are even functions of k_z and $m'(k_z)$, $v'_1(k_z)$, and $v'_2(k_z)$ are the odd functions (see Appendix C for derivation).

TABLE II. Model parameters in Eq. (13) for graphyne-2 and -4 which reproduce the band structure obtained from DFT. The other parameters are set to zero. $N = 4'$ stands for the graphyne-4 under the pressure $P \approx 3.8$ GPa.

N	\tilde{m}_{00}	\tilde{m}_{01}	\tilde{m}_{02}	\tilde{m}_{10}	\tilde{m}_{11}	\tilde{m}_{12}	\tilde{m}'_1	\tilde{m}'_2	\tilde{v}_0/L
2	0	0.125	0	0.213	0.233	0	-0.23	0	0.491
4	0.07	-0.02	-0.02	0.24	-0.16	0.01	0.17	0.17	0.3
4'	0.16	-0.06	-0.1	0.13	-0.36	0.1	0.41	-0.17	0.3

In the Fourier series of k_z , we can write

$$\begin{aligned} m_i(k_z) &= \sum_{q=0} \tilde{m}_{iq} \cos(qk_z d), \\ v(k_z) &= \sum_{q=0} \tilde{v}_q \cos(qk_z d), \\ m'(k_z) &= \sum_{q=1} \tilde{m}'_q \sin(qk_z d), \\ v'_i(k_z) &= \sum_{q=1} \tilde{v}'_q \sin(qk_z d). \end{aligned} \quad (13)$$

The model within the first harmonics (i.e., only the terms with $q \leq 1$) well reproduces the band structure of first-principles calculation [see Fig. 7(a)], by choosing the parameters listed in Table II.

The model without $v'_i(k_z)$ terms in Eq. (12) is equivalent to the effective Hamiltonian derived in Ref. [34]. Actually $v'_i(k_z)$ is irrelevant in the graphyne-2 because the low-energy bands are located near the Z point, where $\sin(k_z d)$ is small. The effective model Eq. (12) also applies to the graphynes with even N 's, which have the same crystal symmetry. Also, the model with k_z -dependent terms neglected (i.e., $\tilde{m}_{iq} = \tilde{v}_q = \tilde{m}'_q = \tilde{v}'_q = 0$ for $q \geq 1$) describes the monolayer graphynes of even N . The fitted parameters for monolayer graphyne $N = 2$ and 4 are given in Table III, which gives the dashed curves in Figs. 2(b) and 2(d).

The model Eq. (12) is analytically solvable. Let us first consider the $k_x = 0$ plane which is invariant under the mirror reflection M_x . The mirror reflection operator acting on the effective Hamiltonian Eq. (12) is given by

$$M_x = S_6^3 C_{2x} = \sigma_x \tau_z. \quad (14)$$

It is diagonalized to $M'_x = U M_x U^\dagger = \tau_z$ by $U = \frac{1}{4}(-\tau_+ \sigma_x + \tau_-)(\tau_x \sigma_+ + \sigma_-) e^{-i(\pi/4)\sigma_y}$, with $\sigma_{\pm} = \sigma_x \pm i\sigma_y$ and $\tau_{\pm} = \tau_x \pm i\tau_y$. By using this unitary transformation, we can block-diagonalize the effective Hamiltonian Eq. (12) as

$$U H(0, k_y, k_z) U^\dagger = H_+ \oplus H_-, \quad (15)$$

TABLE III. Model parameters in Eq. (13) for graphyne-2 and -4 to reproduce the band structure obtained from the DFT calculation.

N	\tilde{m}_{00}	\tilde{m}_{10}	\tilde{v}_0/L
2	0.15	0.2	0.5
4	0.2	0.25	0.3

with

$$H_\eta = m_0 - \eta v'_2 k_y - (m_1 - \eta v'_1 k_y) \sigma_z - (m' - \eta v k_y) \sigma_y, \quad (16)$$

where η indicates the eigenvalue of the mirror operator $\eta(M_x) = \pm 1$. By diagonalizing H_η , the eigenenergy in $k_x = 0$ is obtained as

$$E_{\pm, \eta} = m_0 - \eta v'_2 k_y \pm \sqrt{(m_1 - \eta v'_1 k_y)^2 + (m' - \eta v k_y)^2}. \quad (17)$$

From Eq. (17) we obtain the intersection of the nodal line and the $k_x = 0$ plane. For each sector of $\eta(M_x) = \pm 1$, the gap-closing point on the $k_x = 0$ plane is obtained by $E_{+, \eta} = E_{-, \eta}$, or

$$\begin{cases} m_1(k_z) - \eta v'_1(k_z) k_y = 0, \\ m'(k_z) - \eta v(k_z) k_y = 0. \end{cases} \quad (18)$$

We can show that solutions of Eq. (18) exist when the sign of $m_1(k_z)$ changes between $k_z d = 0$ and π , namely a band inversion of the E_g and E_u state takes place between Γ and Z points. It is clear that if there are solutions of Eq. (18) $\mathbf{k} = \pm(0, k_{y0}, k_{z0})$ for $\eta(M_x) = +1$, we always have other solutions $\mathbf{k} = \pm(0, -k_{y0}, k_{z0})$ for $\eta(M_x) = -1$. In Fig. 7(c), we schematically illustrate such a gap closing with $\eta(M_x) = +1$ and -1 as magenta and blue cones, respectively. In addition, the model Eq. (12) has an effective rotation symmetry

$$H(D_\theta[\mathbf{k}]) = e^{-i\theta\sigma_z/2} H(\mathbf{k}) e^{i\theta\sigma_z/2}, \quad (19)$$

where $D_\theta[\mathbf{k}]$ represents the rotation of \mathbf{k} along the z -axis by angle θ . Therefore, the trajectory of the gap-closing point forms a circle parallel to $k_x k_y$ plane as shown in Figs. 7(b) and 7(c).

Each single-nodal ring cannot disappear in its own even when shrunk to a point. This stability of the nodal line in ABC-graphyne-2 is ensured by a nonzero Z_2 monopole charge defined by the time-reversal and inversion symmetry [35]. Meanwhile, we can also understand this stability by using crystalline symmetry. We see in Fig. 7(c) that the intersection of the horizontal nodal ring and $k_x = 0$ plane forms two Dirac cones in the $k_y k_z$ plane. As these two cones belong to the sectors with opposite mirror eigenvalue $\eta(M_x)$, the mass term is not allowed even when they overlap with each other. To gap out this nodal ring, one needs to merge the two Dirac cones with the same mirror eigenvalues $\eta(M_x)$, as shown in Fig. 8. With changing the model parameter from $m_1(Z) < 0$ to $m_1(Z) > 0$ [from $m_1(\Gamma) > 0$ to $m_1(\Gamma) < 0$] continuously, the Dirac points associated with two nodal rings move along dashed curve in Fig. 8 and annihilate in a pair at the Z (Γ) points when the band inversion of E_g and E_u is removed.

B. ABC stacked graphyne-4

Figure 9(a) shows the energy band for ABC-stacked graphyne-4, which is obtained by a similar DFT calculation with the structural optimization. Unlike the graphyne-2, the graphyne-4 has no band inversion and hence it is a topologically trivial semiconductor. Still, the low-energy band structure can be described by the effective continuum model (12), as it is based on the crystal symmetry of even- N

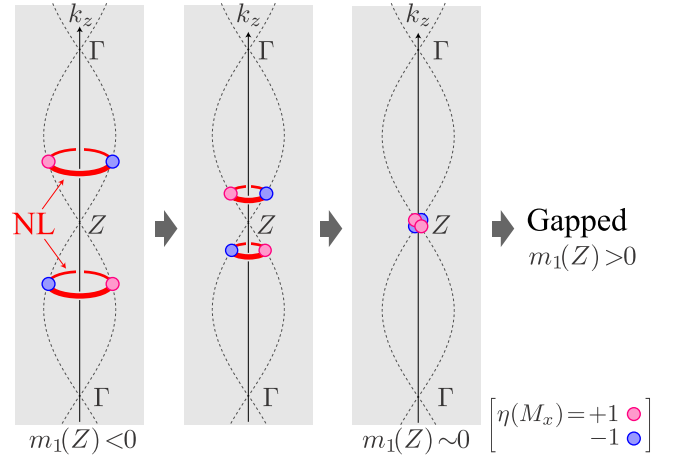


FIG. 8. Pair annihilation of the nodal lines in graphyne-2. Blue and magenta dots represent the Dirac points on $k_x = 0$ plane with $\eta(M_x) = +1$ and -1 , respectively, which are the intersecting points of nodal ring and $k_x = 0$ plane. Dashed curves are the trajectory of the Dirac points towards the pair annihilation at Z point, which is obtained as solutions of the second line of Eq. (18) with $m'(k_z) = u' \sin(k_z d)$ and $v(k_x) = v_0$.

graphyne. In Fig. 9(a), the dashed curves are given by the effective model upto the second harmonics [$q \leq 2$ in Eq. (13)], with the parameters listed in Table II.

In terms of the effective model, the band inversion takes place when $|\tilde{m}_{11}| > |\tilde{m}_{10} + \tilde{m}_{12}|$. The parameter \tilde{m}_{11} represents the interlayer hopping between the neighboring graphyne layers, which occurs in the atomic overlap region illustrated as a dashed circle in Fig. 10. We see that the relative size of the dashed circle to the whole unit cell (hexagon) becomes smaller for larger N , resulting in a weaker interlayer coupling in the electronic system. Due to the smallness of the interlayer coupling (hence that of \tilde{m}_{11}), the graphyne-4 remains a trivial semiconductor.

In van der Waals layered materials, however, the interlayer coupling is highly sensitive to the external pressure, as it reduces the interlayer distance [99–104]. Actually, we can show that applying a pressure to ABC graphyne-4 enhances the interlayer coupling, and causes a topological phase transition to a nodal-line semimetal. To study this effect induced by uniaxial pressure, we carry out the DFT band calculation by changing the interlayer distance d systematically. Under the fixed d , the in-plane lattice constant L and the atomic position are determined to minimize the total energy, and the total energy profile is obtained as a function of d as presented in the inset of Fig. 9(c). We estimate the corresponding pressure by

$$P(d) = -\frac{1}{S} \frac{\partial U}{\partial d}, \quad (20)$$

where U is the numerically obtained total energy and $S = \sqrt{3}L^2/2$ is the size of the unit cell projected on the xy plane. Figure 9(b) shows the band structure of ABC-stacked graphyne-4 under $P \approx 3.8$ GPa. We see that the pressure induces the band inversion between E_g and E_u states at the Γ point, resulting in a \mathbb{Z}_2 nontrivial nodal-line phase similar to graphyne-2. Figure 9(c) shows the relative energy from the

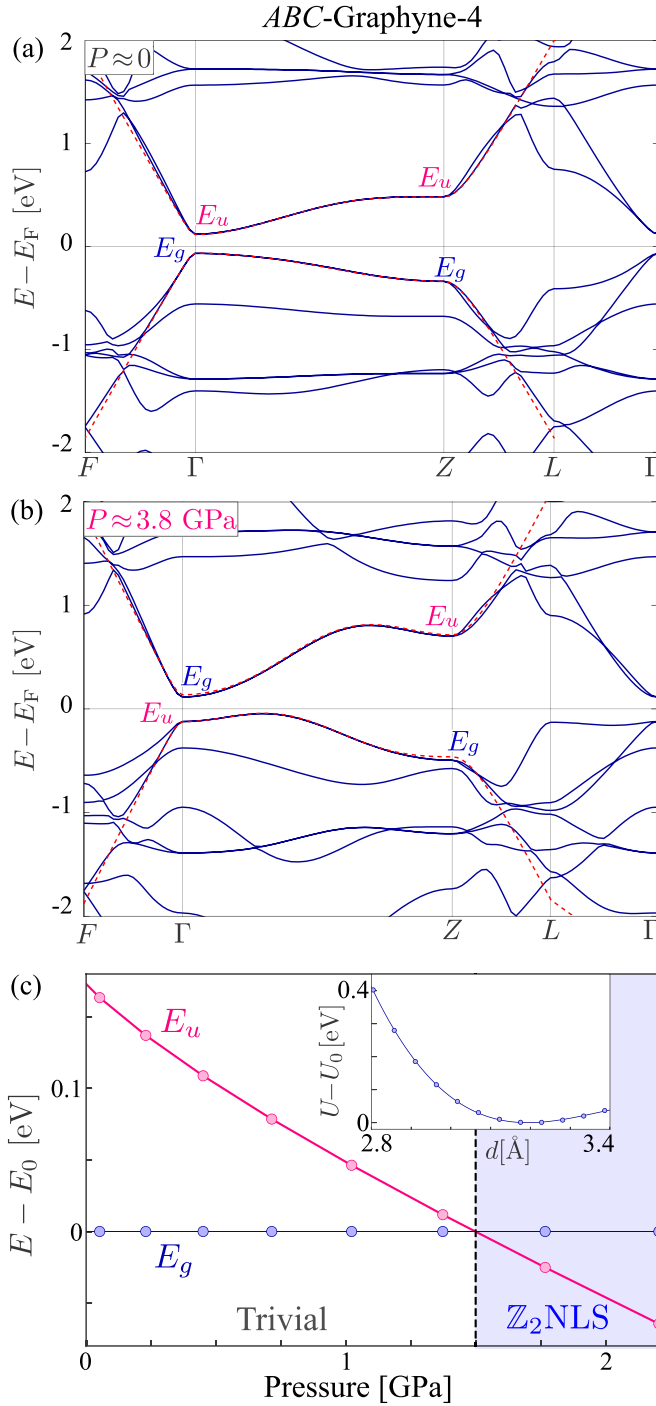


FIG. 9. Energy spectrum of ABC-stacked graphyne-4 obtained from DFT calculation, with interlayer distance (a) $d \approx 3.25$ Å ($P \approx 0$) and (b) 2.66 Å ($P \approx 3.8$ GPa). (c) Energy difference between E_g and E_u states at Γ point as a function of pressure. Inset shows the total energy of the system (measured from its minimum U_0) as a function of the interlayer distance d .

E_g state to E_u state at the Γ point, where we see that the phase transition takes place at $P \approx 1.5$ GPa. The ABC-stacked graphyne-4 is a good platform for the nodal-line semimetal with the \mathbb{Z}_2 monopole controllable by the pressure.

The effective continuum model Eq. (12) can also describe the band structure under pressure. The dashed curve in

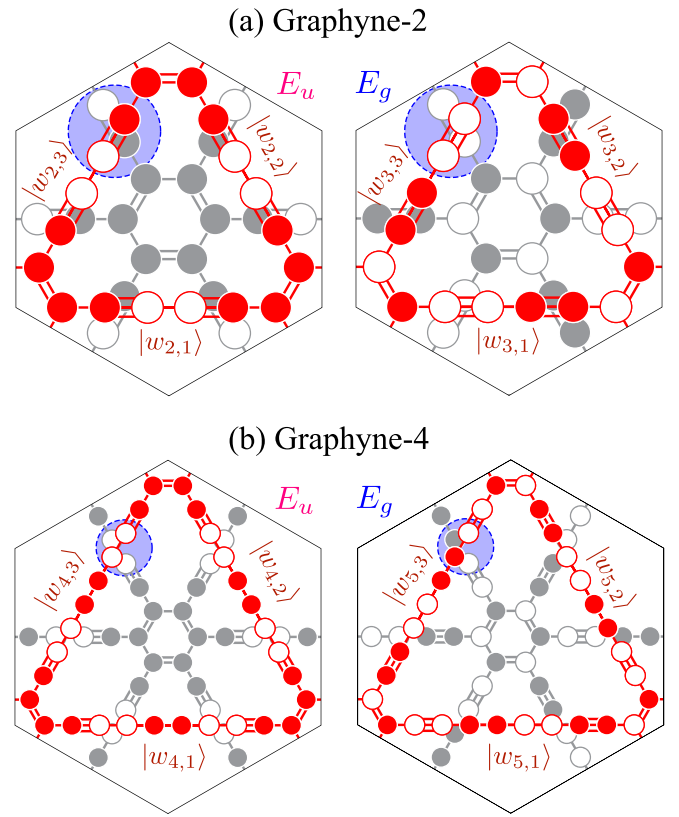


FIG. 10. Atomic structure and wave functions on two neighboring layers of ABC-stacked (a) graphyne-2 and (b) graphyne-4. Red and gray circles represent carbon atoms on layers at $z = +d$ and $z = 0$, respectively, and open and filled circles indicate positive and negative sign of atomic wave function $\psi_n(x_j)$ from Eq. (4). Dashed blue circle represents the atomic overlap region with significant interlayer coupling.

Fig. 9(b) is actually obtained by the parameters as $N = 4'$ in Table II. In the model, the condition for the band inversion $|\tilde{m}_{11}| > |\tilde{m}_{10} + \tilde{m}_{12}|$ is satisfied due to the enhancement of interlayer hopping. We also notice that the pressure distorts the energy bands on the Γ -Z line in Fig. 9, and this is caused by the enhancement of the second harmonics \tilde{m}_{02} and \tilde{m}_{12} , originating from the hopping between the next neighboring layers.

As mentioned, the band inversion of graphyne-4 takes place at the Γ point [Fig. 9(b)], in contrast to graphyne-2 having the inversion at the Z point [Fig. 7(a)]. In the effective model, the position of the band inversion is attributed to the sign of the parameter \tilde{m}_{11} , which is $\tilde{m}_{11} < 0$ for ABC-graphyne-4 while $\tilde{m}_{11} > 0$ for ABC-graphyne-2. The sign of \tilde{m}_{11} is related to the in-plane electronic structure of E_g and E_u states consisting of the Bloch wave function $|w_{N,\alpha}(0)\rangle$ and $|w_{N+1,\alpha}(0)\rangle$ of a 1D chain given by Eq. (6) [see also Fig. 4(c)]. The neighboring interlayer hopping is determined by the relative sign of the wave functions of the two neighboring layers, in an atomic overlap region [dashed circle of Fig. 10]. We see that the relative signs for E_u and E_g states in graphyne-4 are similar to E_g and E_u in graphyne-2, respectively, and it explains the opposite signs of \tilde{m}_{11} for these two cases.

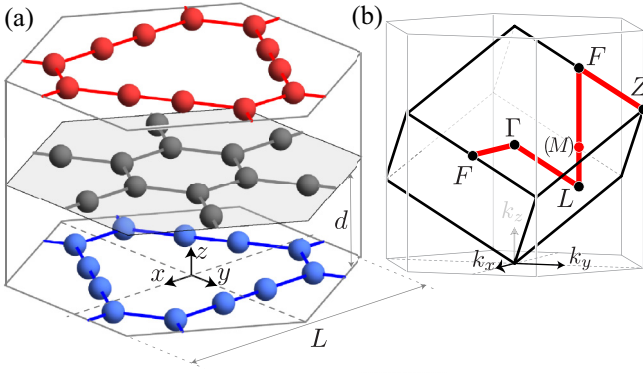


FIG. 11. (a) Lattice structure of ABC-stacked graphyne-1 and (b) the corresponding Brillouin zone.

IV. ABC-STACKED GRAPHYNES (ODD N)

The electronic structure of ABC-stacked graphyne with odd N is completely different from that of even N , due to the even-odd effect in monolayer graphynes. In the following, we study the graphyne-1 and -3 paying attention to the band characteristics and the topological properties.

A. ABC-stacked graphyne-1

As shown in Fig. 11, the lattice structure and the crystal symmetry of ABC-stacked graphyne-1 are the same as those of graphyne-2 except for the length of the 1D chain in Fig. 11(a). The M point of the monolayer Brillouin zone, where the gap minima appear in graphyne-1 (see Figs. 2 and 3), is located on the FL line of the rhombohedral Brillouin zone [Fig. 11(b)].

We optimize the atomic structure and calculate the electronic structure by the DFT band calculation in a similar manner to the systems with even N . Figure 12(a) shows the band structure on the high-symmetry lines depicted in Fig. 11(b). A relatively narrow energy gap around L and F points originates from the minimum gap at the M point in the monolayer graphyne-1. Importantly, we observe a band crossing on the LF and FZ lines, which is a cross section of a nodal line protected by mirror reflection symmetry $M_x = IC_{2x}$. Since the $k_x = 0$ plane is invariant under M_x , the energy bands with the mirror eigenvalues $\eta(M_x) = \pm 1$ do not mix with each other on the plane. In addition, as seen in Fig. 12(a), the energy bands of $\eta(M_x) = \pm 1$ are inverted just near the F point, resulting in a band-crossing ring around F on the $k_x = 0$ plane [Fig. 12(b)]. Due to threefold rotational symmetry, there are three independent nodal rings in the first Brillouin zone.

We derive a two-band effective theory around the F point as follows. The little group at the F point in the rhombohedral Brillouin zone is generated by C_{2x} and I [105]. As F and M share the same in-plane momentum (k_x, k_y) , the lowest-energy states at F originate from B_{3g} and A_u states at M of monolayer graphyne-1 [Fig. 2(a)], which are characterized by parity $[\eta(M_x), \eta(I), \eta(C_{2x})] = (+1, +1, -1)$ and $(-1, -1, -1)$, respectively. We label these lowest-energy states in the three-dimensional system by $|\pm, F\rangle$, where the label \pm corresponds to $\eta(M_x) = \pm 1$, respectively.

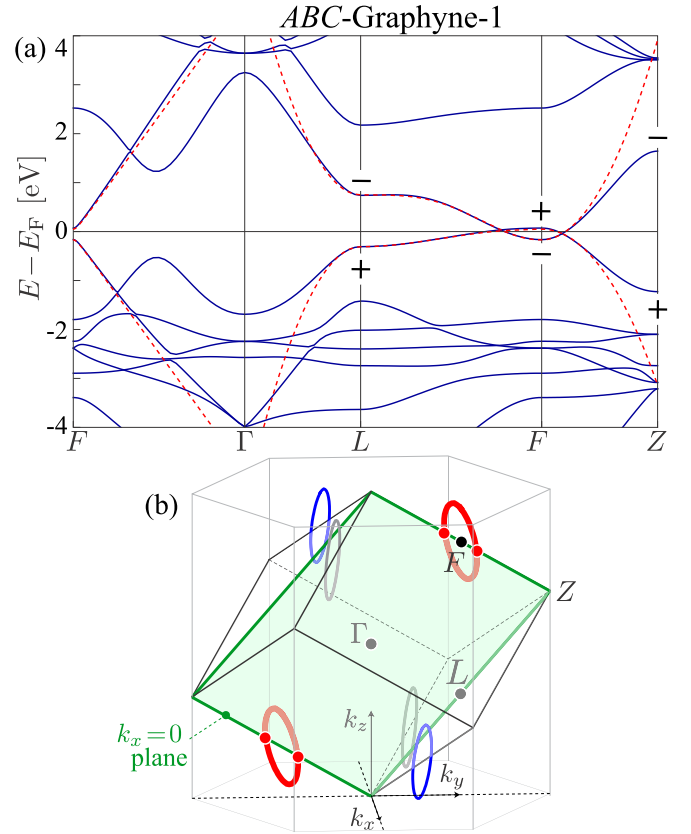


FIG. 12. (a) Band structure of ABC stacked graphyne-1 obtained from the DFT calculation. The dashed line is the dispersion relation calculated by the effective model Eqs. (21) with (25). The sign indicates the mirror parity $\eta_n(M_x) = \pm 1$ at high symmetric points. (b) The nodal line structure in the three-dimensional momentum space. The red, blue, and gray loops are C_{3z} counterparts.

The general form of the two-band effective Hamiltonian is given by

$$H(\tilde{\mathbf{k}}) = \epsilon(\tilde{\mathbf{k}})\sigma_0 + \mathbf{g}(\tilde{\mathbf{k}}) \cdot \boldsymbol{\sigma}, \quad (21)$$

where $\sigma_{\mu=0,x,y,z}$ is the unit and Pauli matrices acting on a two-dimensional basis $|\pm, F\rangle$, $g_{\mu=x,y,z}$ and ϵ are the real numbers. The momentum $\tilde{\mathbf{k}} = [(k_x - k_x^F)L, (k_y - k_y^F)L, (k_z - k_z^F)d]$ is a dimensionless wave vector measured from the F point, $\mathbf{k}^F = 2\pi[0, (\sqrt{3}L)^{-1}, (3d)^{-1}]$, and normalized in units of (L, L, d) for (k_x, k_y, k_z) . In the present system we have time-reversal symmetry given by

$$H^*(\tilde{\mathbf{k}}) = H(-\tilde{\mathbf{k}}). \quad (22)$$

In addition, the inversion symmetry is

$$IH(\tilde{\mathbf{k}})I^{-1} = H(-\tilde{\mathbf{k}}) \quad (23)$$

with $I = \sigma_z$ because the two bases of the present system have opposite inversion parity. The mirror reflection symmetry is

$$M_x H(\tilde{\mathbf{k}}) M_x^{-1} = H(D_{M_x}[\tilde{\mathbf{k}}]), \quad (24)$$

with $M_x = IC_{2x} = \sigma_x$, and $D_{M_x}[\tilde{\mathbf{k}}] = (-\tilde{k}_x, \tilde{k}_y, \tilde{k}_z)$. Equations (22), (23), and (24) yield to the constraints for \mathbf{g}

TABLE IV. Model parameters of Eq. (25) for ABC stacked graphyne-1 and -3 to reproduce the DFT results.

N	E_{00}	E_{01}	E_{02}	B_{00}	D_{01}	E_{z0}	E_{z1}	E_{z2}	B_{z0}	D_{z1}	v/L
1	0.15	-0.14	-0.06	0.01	-0.05	0.26	-0.33	-0.05	-0.33	0.3	0.77
3	0.16	-0.02	-0.03	0.02	-0.07	-0.26	-0.02	0.01	-0.16	0.1	0.36

and ϵ :

$$\begin{aligned}
g_x &= 0, \\
g_y(\tilde{\mathbf{k}}) &= -g_y(-\tilde{\mathbf{k}}) = -g_y(-\tilde{k}_x, \tilde{k}_y, \tilde{k}_z), \\
g_z(\tilde{\mathbf{k}}) &= +g_z(-\tilde{\mathbf{k}}) = +g_z(-\tilde{k}_x, \tilde{k}_y, \tilde{k}_z), \\
\epsilon(\tilde{\mathbf{k}}) &= +\epsilon(-\tilde{\mathbf{k}}) = +\epsilon(-\tilde{k}_x, \tilde{k}_y, \tilde{k}_z).
\end{aligned} \tag{25}$$

Up to the second order of \tilde{k}_x and \tilde{k}_y , they are uniquely determined as

$$\begin{aligned}
g_y &= (v/L)\tilde{k}_x \\
g_z &= \sum_{q=0} [E_{zq} + A_{zq}\tilde{k}_x^2 + B_{zq}\tilde{k}_y^2] \cos(q\tilde{k}_z) + \sum_{q=1} D_{zq}\tilde{k}_y \sin(q\tilde{k}_z), \\
\epsilon &= \sum_{q=0} [E_{0q} + A_{0q}\tilde{k}_x^2 + B_{0q}\tilde{k}_y^2] \cos(q\tilde{k}_z) + \sum_{q=1} D_{0q}\tilde{k}_y \sin(q\tilde{k}_z),
\end{aligned} \tag{26}$$

where $E_{\mu q}$, $A_{\mu q}$, $B_{\mu q}$, $D_{\mu q}$ ($\mu = 0, z$), and v are model parameters. Table IV lists the parameters for the ABC-graphyne-1, which are obtained to fit the DFT band structure [dashed curves in Fig. 12(a)].

Actually, the effective model Eq. (21) applies to ABC-graphynes with any odd N 's since it is derived purely from the symmetry consideration. Also, it is worth noting that the effective model neglecting k_z -dependent (i.e., $q \geq 1$) terms describes the monolayer graphyne of odd N . Table V presents the parameters for monolayer graphyne-1 and -3, which are obtained to give the dashed curves in Figs. 2(a) and 2(c), respectively.

The trajectory of the nodal line can be obtained by $\mathbf{g}(\tilde{\mathbf{k}}) = 0$. As is obvious from Eq. (26), the condition becomes $k_x = 0$ and $g_z = 0$, which gives red nodal loops in Fig. 12(b). On the symmetric plane $k_x = 0$, the vector \mathbf{g} is oriented to either of $\pm z$, and the domain of $g_z > 0$ and that of $g_z < 0$ are separated by the nodal line. On a closed path encircling the nodal line, the vector $\mathbf{g} = (0, g_y, g_z)$ rotates on a g_y - g_z space by an odd number, considering the constraint of Eq. (25). Therefore, the Berry phase on the path is π , which topologically protects the nodal line [37].

TABLE V. Model parameters of Eq. (25) for monolayer stacked graphyne-1 and -3 to reproduce the DFT result.

N	E_{00}	E_{z0}	B_{z0}	v/L
1	0.1	0.2	0.1	0.7
3	0.26	0.3	0.15	0.4

B. ABC-stacked graphyne-3

Finally we discuss the graphyne-3 as an example of the larger odd- N system. Its low-energy effective theory is the same as graphyne-1 and it is given by Eqs. (21) and (26). In Fig. 13(a), we see that the DFT band structure can be fitted by the continuum model (dashed curves) by using the parameters in Table IV. In contrast to graphyne-1, the band inversion does not occur, and this is because the interlayer atomic overlap in graphyne-3 is smaller than in graphyne-1, just in the same manner as the comparison of graphyne-4 to -2.

Figure 13(b) shows the band structure under pressure of $P = 7.1$ GPa. We see that the band inversion between the valence and conduction bands does not occur, but instead the two valence bands cross each other. These two bands are characterized by odd and even mirror parities $\eta(M_x) = -1$ and $+1$, respectively, and hence the band crossing is formed on a closed ring around the F point, similar to the nodal line of graphyne-1 illustrated in Fig. 12(b). The \mathbb{Z}_2 monopole charge of this class of nodal line is trivial just as in graphyne-1. Figure 13(c) shows the energy difference of the highest two valence bands at the F point, where we see that the topological phase transition takes place at $P \approx 4.5$ GPa.

V. SUMMARY

We presented a systematic study on the electronic structures and the topological natures of graphyne- N monolayer and ABC-stacked multilayer. We found an even-odd effect in the N -dependence of the band structure, and in particular, we observed that ABC-stacked graphynes of even and odd N 's support two topologically distinct classes of nodal-line semimetal phases. Specifically, the ABC-graphyne of even N becomes a nodal line semimetal with nontrivial \mathbb{Z}_2 monopole charge, as a consequence of the band inversion of doubly degenerate states in its monolayer counterpart. The ABC graphyne with odd N only also becomes a nodal line semimetal but without \mathbb{Z}_2 monopole charge because it results from a band inversion of nondegenerate conduction and valence bands. ABC graphynes $N = 3$ and 4 become gapped trivial insulators because of smaller interlayer couplings, while we demonstrate that the external pressure induces the topological phase transitions to nodal-line semimetal phases. Therefore, graphynes serve as a novel platform to study the physics of \mathbb{Z}_2 trivial and nontrivial nodal-line semimetals.

ACKNOWLEDGMENTS

This work was supported by JSPS KAKENHI Grants No. JP16K17755, No. JP20K14415, No. JP17K05496, No. JP20H01840, and No. JP20H00127. T.K. is partially supported by JSPS Core-to-Core program and CREST, JST (Grant No. JPMJCR18T4). A part of the numerical calculations was performed on XC40 at YITP at Kyoto University.

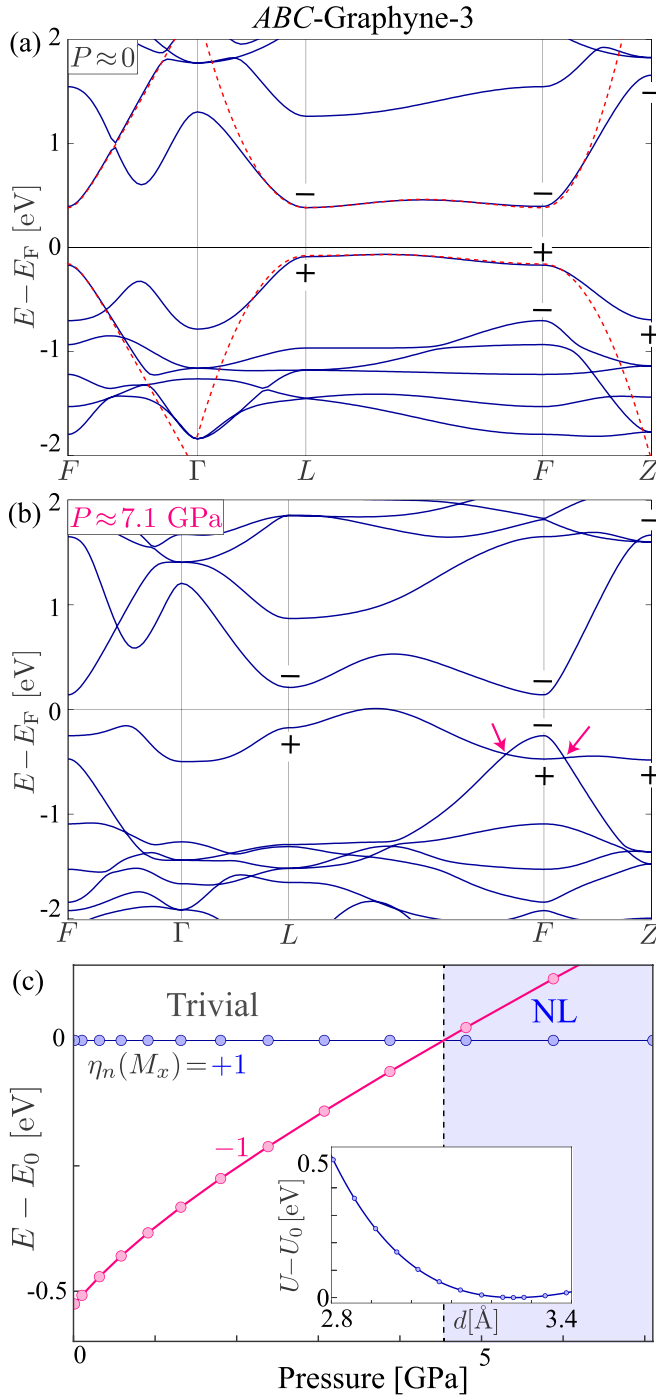


FIG. 13. Energy spectrum of ABC-stacked graphyne-3 obtained from DFT calculation, with interlayer distance (a) $d \approx 3.25$ Å ($P \approx 0$) and (b) 2.66 Å ($P \approx 7.1$ GPa). The sign on bands indicates the mirror parity $\eta_n(M_x) = \pm 1$ at high symmetric points. (c) Energy difference between the two highest valence bands at F point as a function of pressure. Inset shows the total energy of the system (measured from its minimum U_0) as a function of the interlayer distance d .

APPENDIX A: COMPUTATIONAL DETAILS

The DFT calculations in this paper are performed using the first-principle's package QUANTUM ESPRESSO [89]. We

employ the ultrasoft pseudopotentials with Perdew-Zunger self-interaction corrected density functional, the cutoff energy of the plane-wave basis, and the charge density expansion 60 and 300 Ry, respectively, and the convergence criterion of 10^{-8} Ry. We take the wave number mesh as 12×12 for monolayer graphyne $N = 1, 2, 3$, and 4. The meshes taken for ABC-stacked graphynes are $12 \times 12 \times 12$ for $N = 1$ and 2, and $4 \times 4 \times 8$ for $N = 3$ and 4. The atomic structure and lattice structure are optimized by the structural relaxation code in QUANTUM ESPRESSO. Here the criterion for the structural relaxations for total energy convergence and force on atoms are taken as 10^{-5} Ry and 10^{-4} Ry/ a_B with Bohr radius a_B , respectively.

APPENDIX B: SYMMETRY OF EFFECTIVE KAGOME MODEL

Let us consider the electronic property of the effective kagome lattice composed of 1D chain (see Figs. 4 and 5). According to the definition of the Bloch state of the present kagome lattice Eq. (6), the matrix representation of symmetry operator acting on the Bloch Hamiltonian Eq. (7) is given by

$$C_{6z} = \eta_n^{\text{1D}} \begin{pmatrix} 0 & 1 & 0 \\ 0 & 0 & 1 \\ 1 & 0 & 0 \end{pmatrix}, \quad (\text{B1})$$

$$C_{2x} = \begin{pmatrix} -1 & 0 & 0 \\ 0 & 0 & -1 \\ 0 & -1 & 0 \end{pmatrix}, \quad (\text{B2})$$

$$I = -\eta_n^{\text{1D}}, \quad (\text{B3})$$

where η_n^{1D} is the parity of the n th 1D chain state defined in Eq. (5). This implies that the orbital with even (odd) n at each site of the kagome lattice can be regarded as the p_z (d_{xz}) orbital at the kagome cite with the x -axis along the direction of the 1D chain.

Solving the Bloch equation for the Hamiltonian Eq. (7), we obtain the wave function at the Γ point with $E = \epsilon_n + 2t_{\text{eff}}$,

$$\Psi_{n,\pm,0} = \frac{1}{\sqrt{3}}(1, \omega^{\pm 1}, \omega^{\mp 1})^T. \quad (\text{B4})$$

The symmetry characters of this state are given by $C_{6z}\Psi_{n,\pm,0} = \eta_n(C_{6z})\Psi_{n,\pm,0}$ with

$$\eta_n(C_{6z}) = \eta_n^{\text{1D}}\omega^{\pm 1} \quad (\text{B5})$$

and by $I\Psi_{n,\pm,\Gamma} = \eta_n(I)\Psi_{n,\pm,\Gamma}$ with

$$\eta_n(I) = -\eta_n^{\text{1D}}. \quad (\text{B6})$$

These characters for even and odd n correspond to E_{2u} and E_{1g} representations of D_{6h} respectively.

At the M point $(k_x, k_y) = [0, 2\pi/(\sqrt{3}L)] = \mathbf{G}_2/2$ the wave function with eigenenergy $E = \epsilon_n - 2t_{\text{eff}}$ is

$$\Psi_{n,\mathbf{G}_2/2} = \frac{1}{\sqrt{2}}(0, 1, 1)^T. \quad (\text{B7})$$

This momentum is invariant under C_{2x} and I followed by reciprocal lattice translation $V_{-\mathbf{G}_2} =$

$\text{diag}[e^{iG_2 \cdot L_1/2}, e^{iG_2 \cdot L_2/2}, e^{iG_2 \cdot L_3/2}]$, which characterize the wave function as

$$V_{-G_2} I \Psi_{n,G_2/2} = \eta_n(I) \Psi_{n,G_2/2}, \quad (\text{B8})$$

$$V_{-G_2} C_{2x} \Psi_{n,G_2/2} = \eta_n(C_{2x}) \Psi_{n,G_2/2}. \quad (\text{B9})$$

The parity for each operation is then identified as

$$\eta_n(I) = \eta_n^{\text{ID}}, \quad \text{and} \quad \eta_n(C_{2x}) = 1. \quad (\text{B10})$$

These characters for even and odd n correspond to B_{3g} and A_u representations of D_{2h} , respectively.

APPENDIX C: FOUR-BAND EFFECTIVE MODEL OF ABC GGRAPHYNES OF EVEN N

In this section, we derive a low-energy effective model for ABC-stacked graphynes of even N on the basis of symmetry consideration. The Γ and Z points in ABC-stacked graphyne have the highest symmetry D_{3d} in the momentum space, which is generated by improper rotation $S_6 = IC_{3z}$ and twofold rotation C_{2x} . At these momenta, in addition, low-energy states in ABC-stacked graphynes of even N belong to two-dimensional irreducible representations E_g and E_u of D_{3d} and these representations mix with each other in the general momenta away from the Γ and Z points.

We here define the four-dimensional basis as $|\alpha, \beta\rangle$ ($\alpha, \beta = \pm$) and unit and Pauli matrix τ_μ and σ_μ with $\mu = 0, x, y, z$ acting on the 2×2 space spanned by first and second indexes α and β , respectively. More specifically, $|\alpha, \beta\rangle$ are the eigenstates of σ_z and τ_z ,

$$\tau_z |\alpha, \beta\rangle = \alpha |\alpha, \beta\rangle, \quad \text{and} \quad \sigma_z |\alpha, \beta\rangle = \beta |\alpha, \beta\rangle. \quad (\text{C1})$$

Let us consider representations for the generator of the D_{3d} group. Because the E_g (E_u) states consist of the eigenstates of S_6 with eigenvalue $e^{\pm i2\pi/3}$ ($-e^{\pm i2\pi/3}$), we take a representation with

$$S_6 = e^{-i2\pi/3\sigma_z} \tau_z. \quad (\text{C2})$$

The representation of twofold rotation satisfying $C_{2x} S_6 C_{2x}^{-1} = S_6^{-1}$ is then taken as

$$C_{2x} = \sigma_x \tau_0. \quad (\text{C3})$$

We also give the representation of the time-reversal symmetry as

$$\mathcal{T} = \sigma_x \tau_z \mathcal{K} \quad (\text{C4})$$

such that it satisfies $\mathcal{T}^2 = \sigma_0 \tau_0$, $[S_6, \mathcal{T}] = 0$, $[C_{2x}, \mathcal{T}] = 0$. Here, \mathcal{K} is a complex conjugate operator. Note that in the present representation, the first index of basis $\alpha = +$ and $-$ is a label for the E_g and E_u states at the Γ and Z points, and $\beta = \pm$ are the internal degrees of freedom in twofold degeneracy, corresponding to the sign of the angular momentum [see Eq. (C2)]. The representation taken here is not unique and one can use another representation obtained by unitary transformation.

We here consider the effective theory by using this representation. Around the k_z axis, we can formally expand the Hamiltonian as

$$H(\mathbf{k}) = M(k_z) + \mathbf{V}(k_z) \cdot \mathbf{k}_\perp, \quad (\text{C5})$$

TABLE VI. Classification of Hermite basis $h_{\mu\nu} = \sigma_\mu \tau_\nu$ consisting of the 4×4 Hamiltonian by D_{3d} point group symmetry. The columns correspond to irreducible representation of D_{3d} point-group symmetry, parity for C_{2x} rotation, behavior under improper S_6 rotation [see Eqs. (C13) and (C13) for the definition], and the basis matrix.

D_{3d}	C_{2x}	S_6	Basis $h_{\mu\nu} = \sigma_\mu \tau_\nu$
A_{1g}	+	Scalar	h_{00}, h_{0z}
A_{2g}	−	Scalar	h_{z0}, h_{zz}
A_{1u}	+	Pseudoscalar	h_{0x}, h_{0y}
A_{2u}	−	Pseudoscalar	h_{zx}, h_{zy}
E_g	(−, +)	Pseudo vector	$(h_{yz}, -h_{xz}), (h_{y0}, -h_{x0})$
E_u	(+, −)	Vector	$(h_{xx}, h_{yy}), (h_{xy}, h_{yx})$

with $\mathbf{k}_\perp = (k_x, k_y)$, $\mathbf{V} = (V_x, V_y)$. M and V_i are 4×4 Hermite matrices, which can be expanded as

$$X(k_z) = X^{\mu\nu}(k_z) h_{\mu\nu}, \quad (\text{C6})$$

with Hermite basis $h_{\mu\nu} = \sigma_\mu \tau_\nu$, real coefficient $X^{\mu\nu}$, and $X = M, V_x$ or V_y .

Let us narrow down the possible terms of $M(k_z)$ and $\mathbf{V}(k_z)$ to satisfy the symmetry of the present system

$$S_6 H(D_{S_6^{-1}}[\mathbf{k}]) S_6^{-1} = H(\mathbf{k}), \quad (\text{C7})$$

$$C_{2x} H(D_{C_{2x}^{-1}}[\mathbf{k}]) C_{2x}^{-1} = H(\mathbf{k}), \quad (\text{C8})$$

$$\mathcal{T} H(-\mathbf{k}) \mathcal{T}^{-1} = H(\mathbf{k}). \quad (\text{C9})$$

Here the improper rotation S_6 of momentum \mathbf{k} is given by

$$D_{S_6^{-1}} \begin{bmatrix} k_x \\ k_y \end{bmatrix} = D_{C_{6z}^{-1}} \begin{bmatrix} k_x \\ k_y \end{bmatrix} = \frac{1}{2} \begin{pmatrix} 1 & -\sqrt{3} \\ \sqrt{3} & 1 \end{pmatrix} \begin{pmatrix} k_x \\ k_y \end{pmatrix}$$

and

$$D_{S_6^{-1}}[k_z] = -k_z. \quad (\text{C10})$$

First, we consider the \mathbf{k} -conserving symmetry obtained from the combination of Eqs. (C9) and (C7),

$$S_6^3 \mathcal{T} H(\mathbf{k}) (S_6^3 \mathcal{T})^{-1} = H(\mathbf{k}). \quad (\text{C11})$$

This gives the restriction

$$X^{0y} = X^{xy} = X^{yy} = X^{z0} = X^{zx} = X^{zz} = 0 \quad (\text{C12})$$

for all $X = M, V_x$, and V_y .

Next, to consider the symmetry which connects different momentum \mathbf{k} , we classify the basis $h_{\mu\nu}$ to representations of D_{3d} as in Table VI, using Eqs. (C2) and (C3). Under the S_6 operation, each representation behaves as either scalar (pseudoscalar)

$$S_6 h_{\mu\nu} S_6^{-1} = \pm h_{\mu\nu}, \quad (\text{C13})$$

or vector (pseudovector)

$$S_6 \begin{pmatrix} h_{\mu\nu} \\ h_{\mu'\nu'} \end{pmatrix} S_6^{-1} = \pm \frac{1}{2} \begin{pmatrix} 1 & -\sqrt{3} \\ \sqrt{3} & 1 \end{pmatrix} \begin{pmatrix} h_{\mu\nu} \\ h_{\mu'\nu'} \end{pmatrix}. \quad (\text{C14})$$

Here the upper (lower) signs are for scalar and vector (pseudoscalar and pseudovector). In addition, each basis has parity

under C_{2x} rotation,

$$C_{2x}h_{\mu\nu}C_{2x}^{-1} = \pm h_{\mu\nu}. \quad (\text{C15})$$

The term $M(k_z)$ in Eq. (C5) independent of the perpendicular momentum \mathbf{k}_\perp has restrictions,

$$S_6 M(k_z) S_6^{-1} = M(-k_z), \quad (\text{C16})$$

$$C_{2x} M(k_z) C_{2x}^{-1} = M(-k_z). \quad (\text{C17})$$

according to the Eqs. (C7) and (C8). Two types of representations A_{1g} and A_{2u} in Table VI satisfy this condition with coefficients $M^{\mu\nu}(-k_z) = M^{\mu\nu}(k_z)$ and $M^{\mu\nu}(-k_z) = -M^{\mu\nu}(k_z)$, respectively. Therefore, accompanied by Eq. (C12), the possible terms are

$$M(k_z) = m_0 h_{00} + m_1 h_{0z} + m' h_{zy}, \quad (\text{C18})$$

with $m_i(-k_z) = m_i(k_z)$ and $m'(-k_z) = -m'(k_z)$.

The inner product $\mathbf{V}(k_z) \cdot \mathbf{k}_\perp$ in Eq. (C5) should be scalar of S_6 [Eq. (C7)]. As the momentum \mathbf{k}_\perp is the vector under the S_6 operation, \mathbf{V} should be the vector (pseudovector) with coefficient $V^{\mu\nu}(-k_z) = V^{\mu\nu}(k_z)$ [$V^{\mu\nu}(-k_z) = -V^{\mu\nu}(k_z)$]. We see from the Table VI and Eq. (C12) that the possible terms are

$$(V_x, V_y) = v'_1(h_{yz}, -h_{xz}) + v'_2(h_{y0}, -h_{x0}) + v(h_{xx}, h_{yx}), \quad (\text{C19})$$

with $v(-k_z) = v(k_z)$ and $v'_i(-k_z) = -v'_i(k_z)$.

Finally, summarizing Eqs. (C18) and (C19) and using Pauli matrices σ_μ and τ_ν , the possible form of the effective Hamiltonian is

$$H(\mathbf{k}) = m_0 + m_1 \sigma_z + m' \sigma_z \tau_y + v \tau_x (\sigma_x k_x + \sigma_y k_y) + (v'_1 + v'_2 \tau_z) (\sigma_y k_x - \sigma_x k_y). \quad (\text{C20})$$

-
- [1] A. H. Castro Neto, F. Guinea, N. M. R. Peres, K. S. Novoselov, and A. K. Geim, *Rev. Mod. Phys.* **81**, 109 (2009).
 - [2] P. R. Wallace, *Phys. Rev.* **71**, 622 (1947).
 - [3] J. C. Slonczewski and P. R. Weiss, *Phys. Rev.* **109**, 272 (1958).
 - [4] P. P. K. Smith and P. R. Buseck, *Science* **216**, 984 (1982).
 - [5] W. P. Su, J. R. Schrieffer, and A. J. Heeger, *Phys. Rev. Lett.* **42**, 1698 (1979).
 - [6] M. J. Rice, A. R. Bishop, and D. K. Campbell, *Phys. Rev. Lett.* **51**, 2136 (1983).
 - [7] M. Koshino, *Phys. Rev. B* **88**, 115409 (2013).
 - [8] L. Ju, Z. Shi, N. Nair, Y. Lv, C. Jin, J. Velasco, C. Ojeda-Aristizabal, H. A. Bechtel, M. C. Martin, A. Zettl, J. Analytis, and F. Wang, *Nature* **520**, 650 (2015).
 - [9] L. J. Yin, H. Jiang, J. B. Qiao, and L. He, *Nat. Commun.* **7**, 11760 (2016).
 - [10] S. Slizovskiy, E. McCann, M. Koshino, and V. I. Fal'ko, *Commun. Phys.* **2**, 164 (2019).
 - [11] T. Cao, F. Zhao, and S. G. Louie, *Phys. Rev. Lett.* **119**, 076401 (2017).
 - [12] D. J. Rizzo, G. Veber, T. Cao, C. Bronner, T. Chen, F. Zhao, H. Rodriguez, S. G. Louie, M. F. Crommie, and F. R. Fischer, *Nature* **560**, 204 (2018).
 - [13] G. Tamaki, T. Kawakami, and M. Koshino, *Phys. Rev. B* **101**, 205311 (2020).
 - [14] W. Izumida, R. Okuyama, A. Yamakage, and R. Saito, *Phys. Rev. B* **93**, 195442 (2016).
 - [15] Y. Chen, Y. Xie, S. A. Yang, H. Pan, F. Zhang, M. L. Cohen, and S. Zhang, *Nano Lett.* **15**, 6974 (2015).
 - [16] A. Rüegg, S. Coh, and J. E. Moore, *Phys. Rev. B* **88**, 155127 (2013).
 - [17] H. C. Po, L. Zou, A. Vishwanath, and T. Senthil, *Phys. Rev. X* **8**, 031089 (2018).
 - [18] J. Ahn, S. Park, and B.-J. Yang, *Phys. Rev. X* **9**, 021013 (2019).
 - [19] M. Koshino, *Phys. Rev. B* **99**, 235406 (2019).
 - [20] P. Moon and M. Koshino, *Phys. Rev. B* **85**, 195458 (2012).
 - [21] Z. Song, Z. Wang, W. Shi, G. Li, C. Fang, and B. A. Bernevig, *Phys. Rev. Lett.* **123**, 036401 (2019).
 - [22] M. J. Park, Y. Kim, G. Y. Cho, and S. B. Lee, *Phys. Rev. Lett.* **123**, 216803 (2019).
 - [23] Y. Chen, Y. Xie, X. Yan, M. L. Cohen, and S. Zhang, *Phys. Rep.* **868**, 1 (2020).
 - [24] A. Bouhon, A. M. Black-Schaffer, and R. J. Slager, *Phys. Rev. B* **100**, 195135 (2019).
 - [25] R. H. Baughman, H. Eckhardt, and M. Kertesz, *J. Chem. Phys.* **87**, 6687 (1987).
 - [26] Q. Peng, J. Crean, L. Han, S. Liu, X. Wen, S. De, and A. Dearden, *Nanotechnol. Sci. Appl.* **7**, 1 (2014).
 - [27] N. Narita, S. Nagai, S. Suzuki, and K. Nakao, *Phys. Rev. B* **58**, 11009 (1998).
 - [28] N. Narita, S. Nagai, S. Suzuki, and K. Nakao, *Phys. Rev. B* **62**, 11146 (2000).
 - [29] D. Malko, C. Neiss, F. Viñes, and A. Görling, *Phys. Rev. Lett.* **108**, 086804 (2012).
 - [30] A. R. Puigdollers, G. Alonso, and P. Gamallo, *Carbon* **96**, 879 (2016).
 - [31] H. Kim, Y. Kim, J. Kim, and W. Y. Kim, *Carbon* **98**, 404 (2016).
 - [32] G. Li, Y. Li, H. Liu, Y. Guo, Y. Li, and D. Zhu, *Chem. Commun.* **46**, 3256 (2010).
 - [33] R. Matsuoka, R. Sakamoto, K. Hoshiko, S. Sasaki, H. Masunaga, K. Nagashio, and H. Nishihara, *J. Am. Chem. Soc.* **139**, 3145 (2017).
 - [34] T. Nomura, T. Habe, R. Sakamoto, and M. Koshino, *Phys. Rev. Mater.* **2**, 054204 (2018).
 - [35] J. Ahn, D. Kim, Y. Kim, and B.-J. Yang, *Phys. Rev. Lett.* **121**, 106403 (2018).
 - [36] C. Fang, Y. Chen, H.-Y. Kee, and L. Fu, *Phys. Rev. B* **92**, 081201(R) (2015).
 - [37] C. Fang, H. Weng, X. Dai, and Z. Fang, *Chin. Phys. B* **25**, 117106 (2016).
 - [38] A. A. Burkov, M. D. Hook, and L. Balents, *Phys. Rev. B* **84**, 235126 (2011).
 - [39] L. Lu, L. Fu, J. D. Joannopoulos, and M. Soljačić, *Nat. Photon.* **7**, 294 (2013).

- [40] Y. Chen, Y.-M. Lu, and H.-Y. Kee, *Nat. Commun.* **6**, 6593 (2015).
- [41] H.-S. Kim, Y. Chen, and H.-Y. Kee, *Phys. Rev. B* **91**, 235103 (2015).
- [42] H. Weng, Y. Liang, Q. Xu, R. Yu, Z. Fang, X. Dai, and Y. Kawazoe, *Phys. Rev. B* **92**, 045108 (2015).
- [43] K. Mullen, B. Uchoa, and D. T. Glatzhofer, *Phys. Rev. Lett.* **115**, 026403 (2015).
- [44] Y. Kim, B. J. Wieder, C. L. Kane, and A. M. Rappe, *Phys. Rev. Lett.* **115**, 036806 (2015).
- [45] R. Yu, H. Weng, Z. Fang, X. Dai, and X. Hu, *Phys. Rev. Lett.* **115**, 036807 (2015).
- [46] T. T. Heikkilä and G. E. Volovik, *New J. Phys.* **17**, 093019 (2015).
- [47] A. Yamakage, Y. Yamakawa, Y. Tanaka, and Y. Okamoto, *J. Phys. Soc. Jpn.* **85**, 013708 (2016).
- [48] G. Bian, T.-R. Chang, R. Sankar, S.-Y. Xu, H. Zheng, T. Neupert, C.-K. Chiu, S.-M. Huang, G. Chang, I. Belopolski, D. S. Sanchez, M. Neupane, N. Alidoust, C. Liu, B. K. Wang, C.-C. Lee, H.-T. Jeng, C. Zhang, Z. Yuan, S. Jia, A. Bansil, F. Chou, H. Lin, and M. Zahid Hasan, *Nat. Commun.* **7**, 10556 (2016).
- [49] J.-T. Wang, H. Weng, S. Nie, Z. Fang, Y. Kawazoe, and C. Chen, *Phys. Rev. Lett.* **116**, 195501 (2016).
- [50] M. Neupane, I. Belopolski, M. M. Hosen, D. S. Sanchez, R. Sankar, M. Szlowska, S.-Y. Xu, K. Dimitri, N. Dhakal, P. Maldonado, P. M. Oppeneer, D. Kaczorowski, F. Chou, M. Zahid Hasan, and T. Durakiewicz, *Phys. Rev. B* **93**, 201104(R) (2016).
- [51] L. M. Schoop, M. N. Ali, C. Straßer, A. Topp, A. Varykhalov, D. Marchenko, V. Duppel, S. S. P. Parkin, B. V. Lotsch, and C. R. Ast, *Nat. Commun.* **7**, 11696 (2016).
- [52] R. Li, H. Ma, X. Cheng, S. Wang, D. Li, Z. Zhang, Y. Li, and X.-Q. Chen, *Phys. Rev. Lett.* **117**, 096401 (2016).
- [53] M. Koshino and I. F. Hizbullah, *Phys. Rev. B* **93**, 045201 (2016).
- [54] B. Lian and S.-C. Zhang, *Phys. Rev. B* **94**, 041105(R) (2016).
- [55] M. Ezawa, *Phys. Rev. Lett.* **116**, 127202 (2016).
- [56] H. Huang, J. Liu, D. Vanderbilt, and W. Duan, *Phys. Rev. B* **93**, 201114(R) (2016).
- [57] T. Hyart and T. T. Heikkilä, *Phys. Rev. B* **93**, 235147 (2016).
- [58] Z. Zhu, G. W. Winkler, Q. S. Wu, J. Li, and A. A. Soluyanov, *Phys. Rev. X* **6**, 031003 (2016).
- [59] D. Takane, Z. Wang, S. Souma, K. Nakayama, C. X. Trang, T. Sato, T. Takahashi, and Y. Ando, *Phys. Rev. B* **94**, 121108(R) (2016).
- [60] T. Bzdušek, Q. Wu, A. Rüegg, M. Sigrist, and A. A. Soluyanov, *Nature* **538**, 75 (2016).
- [61] J. Zhao, R. Yu, H. Weng, and Z. Fang, *Phys. Rev. B* **94**, 195104 (2016).
- [62] Q. Xu, R. Yu, Z. Fang, X. Dai, and H. Weng, *Phys. Rev. B* **95**, 045136 (2017).
- [63] Y. Du, F. Tang, D. Wang, L. Sheng, E.-J. Kan, C.-G. Duan, S. Y. Savrasov, and X. Wan, *npj Quant. Mater.* **2**, 3 (2017).
- [64] X. Zhang, Z.-M. Yu, X.-L. Sheng, H. Y. Yang, and S. A. Yang, *Phys. Rev. B* **95**, 235116 (2017).
- [65] M. Hirayama, R. Okugawa, T. Miyake, and S. Murakami, *Nat. Commun.* **8**, 14022 (2017).
- [66] T. Kawakami and X. Hu, *Phys. Rev. B* **96**, 235307 (2017).
- [67] W. Chen, H.-Z. Lu, and J.-M. Hou, *Phys. Rev. B* **96**, 041102(R) (2017).
- [68] Z. Yan, R. Bi, H. Shen, L. Lu, S.-C. Zhang, and Z. Wang, *Phys. Rev. B* **96**, 041103(R) (2017).
- [69] M. Ezawa, *Phys. Rev. B* **96**, 041202(R) (2017).
- [70] P.-Y. Chang and C.-H. Yee, *Phys. Rev. B* **96**, 081114(R) (2017).
- [71] L. Li, S. Chesi, C. Yin, and S. Chen, *Phys. Rev. B* **96**, 081116(R) (2017).
- [72] G. Chang, S.-Y. Xu, X. Zhou, S.-M. Huang, B. Singh, B. Wang, I. Belopolski, J. Yin, S. Zhang, A. Bansil, H. Lin, and M. Zahid Hasan, *Phys. Rev. Lett.* **119**, 156401 (2017).
- [73] R. Bi, Z. Yan, L. Lu, and Z. Wang, *Phys. Rev. B* **96**, 201305(R) (2017).
- [74] X. Feng, C. Yue, Z. Song, Q. S. Wu, and B. Wen, *Phys. Rev. Mater.* **2**, 014202 (2018).
- [75] D. Takane, K. Nakayama, S. Souma, T. Wada, Y. Okamoto, K. Takenaka, Y. Yamakawa, A. Yamakage, T. Mitsuhashi, K. Horiba, H. Kumigashira, T. Takahashi, and T. Sato, *npj Quant. Mater.* **3**, 1 (2018).
- [76] W. Gao, B. Yang, B. Tremain, H. Liu, Q. Guo, L. Xia, A. P. Hibbins, and S. Zhang, *Nat. Commun.* **9**, 950 (2018).
- [77] C. Gong, Y. Xie, Y. Chen, H.-S. Kim, and D. Vanderbilt, *Phys. Rev. Lett.* **120**, 106403 (2018).
- [78] V. I. Gavrilenko, A. A. Perov, A. P. Protogenov, R. V. Turkevich, and E. V. Chulkov, *Phys. Rev. B* **97**, 115204 (2018).
- [79] Y. Zhou, F. Xiong, X. Wan, and J. An, *Phys. Rev. B* **97**, 155140 (2018).
- [80] Q. Yan, R. Liu, Z. Yan, B. Liu, H. Chen, Z. Wang, and L. Lu, *Nat. Phys.* **14**, 461 (2018).
- [81] M. Hirayama, S. Matsuishi, H. Hosono, and S. Murakami, *Phys. Rev. X* **8**, 031067 (2018).
- [82] T. Nakamura, S. Souma, Z. Wang, K. Yamauchi, D. Takane, H. Oinuma, K. Nakayama, K. Horiba, H. Kumigashira, T. Oguchi, T. Takahashi, Y. Ando, and T. Sato, *Phys. Rev. B* **99**, 245105 (2019).
- [83] S. Jeon, Y.-T. Oh, and Y. Kim, *Phys. Rev. B* **100**, 035406 (2019).
- [84] R. Li, J. Li, L. Wang, J. Liu, H. Ma, H.-F. Song, D. Li, Y. Li, and X.-Q. Chen, *Phys. Rev. Lett.* **123**, 136802 (2019).
- [85] Z. Wang, B. J. Wieder, J. Li, B. Yan, and B. A. Bernevig, *Phys. Rev. Lett.* **123**, 186401 (2019).
- [86] M. Ezawa, *Sci. Rep.* **9**, 5286 (2019).
- [87] H. Li, C. Fang, and K. Sun, *Phys. Rev. B* **100**, 195308 (2019).
- [88] Y. Zhou, F. Xiong, W. Chen, and J. An, *Phys. Rev. B* **101**, 075125 (2020).
- [89] P. Giannozzi, S. Baroni, N. Bonini, M. Calandra, R. Car, C. Cavazzoni, D. Ceresoli, G. L. Chiarotti, M. Cococcioni, I. Dabo, A. Dal Corso, S. Fabris, G. Fratesi, S. de Gironcoli, R. Gebauer, U. Gerstmann, C. Gougoussis, A. Kokalj, M. Lazzeri, L. Martin-Samos, N. Marzari, F. Mauri, R. Mazzarello, S. Paolini, A. Pasquarello, L. Paulatto, C. Sbraccia, S. Scandolo, G. Sclauzero, A. P. Seitsonen, A. Smogunov, P. Umari, and R. M. Wentzcovitch, *J. Phys.: Condens. Matter* **21**, 395502 (2009).
- [90] J. C. Slater and G. F. Koster, *Phys. Rev.* **94**, 1498 (1954).
- [91] T. Nakanishi and T. Ando, *J. Phys. Soc. Jpn.* **70**, 1647 (2001).

- [92] P. Moon and M. Koshino, [Phys. Rev. B](#) **87**, 205404 (2013).
- [93] T. Mizoguchi, M. Maruyama, S. Okada, and Y. Hatsugai, [Phys. Rev. Mater.](#) **3**, 114201 (2019).
- [94] E. Lee, R. Kim, J. Ahn, and B. J. Yang, [npj Quant. Mater.](#) **5**, 1 (2020).
- [95] L.-H. Wu and X. Hu, [Sci. Rep.](#) **6**, 24347 (2016).
- [96] T. Kariyado and X. Hu, [Sci. Rep.](#) **7**, 16515 (2017).
- [97] L.-H. Wu and X. Hu, [Phys. Rev. Lett.](#) **114**, 223901 (2015).
- [98] L. Fu and C. L. Kane, [Phys. Rev. B](#) **76**, 045302 (2007).
- [99] J. E. Proctor, E. Gregoryanz, K. S. Novoselov, M. Lotya, J. N. Coleman, and M. P. Halsall, [Phys. Rev. B](#) **80**, 073408 (2009).
- [100] J. Nicolle, D. Machon, P. Poncharal, O. Pierre-Louis, and A. San-Miguel, [Nano Lett.](#) **11**, 3564 (2011).
- [101] M. Yankowitz, K. Watanabe, T. Taniguchi, P. San-Jose, and B. J. LeRoy, [Nat. Commun.](#) **7**, 13168 (2016).
- [102] Y. Chen, F. Ke, P. Ci, C. Ko, T. Park, S. Saremi, H. Liu, Y. Lee, J. Suh, L. W. Martin, J. W. Ager, B. Chen, and J. Wu, [Nano Lett.](#) **17**, 194 (2017).
- [103] M. Yankowitz, J. Jung, E. Laksono, N. Leconte, B. L. Chittari, K. Watanabe, T. Taniguchi, S. Adam, D. Graf, and C. R. Dean, [Nature](#) **557**, 404 (2018).
- [104] M. Yankowitz, S. Chen, H. Polshyn, Y. Zhang, K. Watanabe, T. Taniguchi, D. Graf, A. F. Young, and C. R. Dean, [Science](#) **363**, 1059 (2019).
- [105] C. Bradley and A. Cracknell, *The Mathematical Theory of Symmetry in Solids: Representation Theory for Point Groups and Space Groups* (Oxford University Press, New York, 2010).